Interfacial Electron Transfer in TiO_2 Surfaces Sensitized with Ru(II)−Polypyridine Complexes†

Elena Jakubikova,‡ Robert C. Snoeberger III,§ Victor S. Batista,§ Richard L. Martin,‡ and Enrique R. Batista*,‡

Theoretical Division, Los Alamos National Laboratory, MS-B268, Los Alamos, New Mexico 87545, and Department of Chemistry, Yale University, P.O. Box 208107, New Haven, Connecticut 06520-8107

Received: April 29, 2009; Revised Manuscript Received: June 19, 2009

Studies of interfacial electron transfer (IET) in TiO_2 surfaces functionalized with (**1**) pyridine-4-phosphonic acid, (**2**) $[Ru(tpy)(tpy(PO_3H_2))]^{2+}$, and (**3**) $[Ru(tpy)(bpy)(H_2O)-Ru(tpy)(tpy(PO_3H_2))]^{4+}$ (tpy = 2,2′:6,2″-terpyridine; bpy = 2,2′-bipyridine) are reported. We characterize the electronic excitations, electron injection time scales, and interfacial electron transfer (IET) mechanisms through phosphonate anchoring groups. These are promising alternatives to the classic carboxylates of conventional dye-sensitized solar cells since they bind more strongly to TiO_2 surfaces and form stable covalent bonds that are unaffected by humidity. Density functional theory calculations and quantum dynamics simulations of IET indicate that electron injection in **1**−TiO_2 can be up to 1 order of magnitude faster when **1** is attached to TiO_2 in a bidentate mode ($\tau \sim 60$ fs) than when attached in a monodentate motif ($\tau \sim 460$ fs). The IET time scale also depends strongly on the properties of the sensitizer as well as on the nature of the electronic excitation initially localized in the adsorbate molecule. We show that IET triggered by the visible light excitation of **2**−TiO_2 takes 1−10 ps when **2** is attached in a bidentate mode, a time comparable to the lifetime of the excited electronic state. IET due to visible-light photoexcitation of **3**−TiO_2 is slower, since the resulting electronic excitation remains localized in the tpy−tpy bridge that is weakly coupled to the electronic states of the conduction band of TiO_2. These results are particularly valuable to elucidate the possible origin of IET efficiency drops during photoconversion in solar cells based on Ru(II)−polypyridine complexes covalently attached to TiO_2 thin films with phosphonate linkers.

Introduction

Understanding the photophysics of transition metal complexes attached to semiconductor surfaces is essential for the design of artificial systems for solar energy conversion. In particular, ruthenium polypyridyl complexes have attracted a great deal of attention as a promising class of compounds with long-lived charge-separated states and rich photochemical properties.[1] However, their electronic excitations and photoconversion mechanisms remain only partially understood. This paper builds upon our recent work[2−9] and addresses the study of TiO_2 nanoparticles sensitized with (**1**) pyridine-4-phosphonic acid, (**2**) $[Ru(tpy)(tpy(PO_3H_2))]^{2+}$, and (**3**) $[Ru(tpy)(bpy)(H_2O)-Ru(tpy)(tpy(PO_3H_2))]^{4+}$ (tpy = 2,2′:6,2″-terpyridine; bpy = 2,2′-bipyridine). Our study includes the characterization of the electronic excitations, electron injection time scales, and mechanisms according to density functional theory (DFT) calculations and quantum dynamics simulations of interfacial electron transfer (IET).

Ruthenium polypyridyl complexes covalently attached to nanoporous wide band gap semiconductors have been extensively investigated because of their potential application to dye-sensitized solar cells.[10−21] In fact, the most efficient dye sensitized solar cell (DSSC) reported to date (with ∼11% efficiency of solar-to-electric energy conversion) is based on Ru(II)−polypyridine complexes (e.g., RuN3 = *cis*-$Ru(dcbpy)_2(NCS)_2$, with dcbpy = 2,2′-bipyridine-4,4′-COOH) attached to TiO_2 thin films through carboxylate groups.[12,22] Remarkably, phosphonate groups bind more strongly to metal oxide surfaces than carboxylates and therefore have attracted significant attention as candidates for more robust molecular assemblies. However, cells based on phosphonate groups attaching Ru(II)−polypyridine complexes (e.g., RuN3P = *cis*-$Ru(bpbpyH_2)_2(NCS)_2$, with bpbpy = 2,2′-bipyridine-4,4′-PO_3H_2) are typically ∼30% less efficient than their corresponding carboxylate analogs.[23] The molecular/electronic origins of the efficiency drops remain poorly understood. Here, we focus on TiO_2 surfaces modified by Ru(II)−polypyridine complexes attached by phosphonate linkers. Emphasis is given to the characterization of the electronic excitations and injection time scales as determined by the nature of the molecular adsorbates and the attachment modes.

In addition to applications in photovoltaic cells for solar-to-electric energy conversion, Ru(II)−polypyridine complexes attached to TiO_2 surfaces by phosphonate linkers resist humidity and can mimic photosynthetic charge transfer events.[2,24−30] Therefore, elucidating the nature of electron transfer mechanisms should impact the development of multicomponent molecular assemblies for photocatalysis and artificial photosynthesis.[31−33]

Visible-light photoexcitation of molecular adsorbates attached to semiconductor surfaces often leads to ultrafast (subpicosecond) IET. While the overall injection process can be probed by ultrafast transient absorption spectroscopy,[34] several competing processes may interfere with IET and mask the spectroscopic features associated with ultrafast IET. Some of these processes

† Part of the "Russell M. Pitzer Festschrift.

* Corresponding author. E-mail: erb@lanl.gov.
‡ Los Alamos National Laboratory.
§ Yale University.

10.1021/jp903966n CCC: $40.75
Published on Web 07/13/2009

include intersystem crossing into low-lying electronic excited states, electronic transitions back to the ground electronic state, and recombination dynamics. In particular, intersystem crossing in ruthenium complexes is thought to play an important role since low lying triplet states of metal-to-ligand charge transfer (MLCT) type can have lifetimes as long as 250 ps at room temperature.[35] The IET from these low lying triplet states is usually slow (50−1000 ps),[34] due to the small density of states at the edge of the conduction band.[36−41] However, the ultrafast kinetics of intersystem crossing can still mask the IET dynamics as probed by transient absorption spectroscopy, making it difficult to characterize the ultrafast IET times from a cursory examination of the experimental data. Therefore, it is essential to combine experimental studies with quantum dynamics simulations of the underlying relaxation processes.

In this paper we analyze IET from $[Ru(tpy)_2]^{2+}$, as well as from its complex with the catalyst $[Ru(tpy)(bpy)(H_2O)]^{2+}$,[42] forming the dimer $[Ru(tpy)(bpy)(H_2O)-Ru(tpy)_2]^{4+}$, when attached to TiO_2−anatase with phosphonate linkers. $[Ru(tpy)_2]^{2+}$ is particularly valuable, due to its linear directionality and has already been applied in molecular assemblies[43] and dye-sensitized solar cells.[19,44] The covalent attachment with phosphonate linkers specifically addresses the possibility of achieving more functionalization of semiconductor surfaces than attainable with carboxylate groups.[45−47]

Previous theoretical work has focused on the comparative analysis of binding energies and vertical excitations when covalently attaching $[Ru(tpy)_2]^{2+}$ to TiO_2 by using carboxylates, or phosphonate linkers.[48] In addition, similar work has been reported for the attachment of pyridine,[49,50] and other dye-sensitized TiO_2 nanoparticles.[51−54] Electron injection rates were estimated, within the framework of the time-independent picture, from the analysis of the overlap of donor and acceptor orbitals in the adsorbate and host-nanoparticle.[48,50] Here, we analyze the time scales and mechanisms of IET according to explicit quantum dynamics simulations, as in previous studies of electron injection in sensitized TiO_2 semiconductors.[5−9] The reported results provide fundamental insight on the electronic and structural properties of molecular assemblies that are important for efficient IET in catalyst-chromophore/TiO_2 interfaces.

The paper is organized as follows. First, we outline the preparation of model adsorbate/TiO_2 supercells, and the computational methods applied for computations of photoabsorption spectra and molecular dynamics simulations of IET. Then, we present the results followed by a comparative analysis of the electronic structure of the various systems investigated. The final section summarizes and concludes.

Methodology

Geometry Optimization. Model systems were obtained by geometry optimization at the density functional theory (DFT) level, using the Vienna Ab Initio Simulation Package (VASP).[55,56] First, the unit cell of bulk TiO_2 was optimized by using periodic boundary conditions (PBC) and the Perdew−Burke−Ernzerhof (PBE) exchange−correlation functional,[57] along with the Projector Augmented-Wave method.[58,59] The energy cutoff of the plane wave expansion was set to 400 eV. The TiO_2 unit cell[60] was relaxed using a (13 × 13 × 13) k-point sampling, resulting in the lattice constants $a = b = 3.83$ Å and $c = 9.61$ Å. Next, the optimized geometry of the TiO_2 unit cell was used to construct a ∼10 Å slab model of the (101) TiO_2 surface functionalized with **1** in vacuum. The upper layers (i.e., top 2 layers of Ti, top 4 layers of O, and **1** attached in a monodentate, or bidentate, mode) were reoptimized using a (5 × 3 × 1) k-point sampling, keeping the supercell volume fixed with lattice vectors $a = 10.35$ Å, $b = 15.33$ Å, and $c = 26.00$, 27.00 Å (monodentate, bidentate attachment). The bottom layers were kept fixed to mimic the properties of bulk TiO_2.

Models of (101) TiO_2 surfaces, functionalized with **2** or **3**, were constructed by first relaxing the configurations of **2** and **3** at the PBE0 level of theory,[61] as implemented in Gaussian 03,[62] with the LANL08 basis set[63,64] on Ru, and the 6-31G* basis set[65,66] on all other atoms, keeping fixed coordinates for the phosphonate functional group and three C atoms in the pyridine ring of the pyridine-4-phosphonate linker as in the relaxed configuration of the (101) TiO_2 surface functionalized with **1**. The resulting configurations of the adsorbates were then attached to the relaxed **1**−TiO_2 surface by overlapping their pyridine-4-phosphonate functional groups with **1** on the surface. For comparison, the geometries of **2** and **3** were also optimized in vacuum using the same level of theory, DFT functional, and basis sets.

Excited States and Absorption Spectra. Vertical excitation energies associated with the singlet electronic excited states of **2** and **3** were obtained at the TD-DFT[67−69] level, using the PBE0 functional and the combination of basis sets described in the previous section. A representation of the virtual and occupied orbitals involved in the electronic transitions was obtained by using the natural transition orbital analysis.[70,71] Absorption spectra were simulated by convoluting the spectrum composed of the δ-functions at the excitation energies times the oscillator strengths with a Gaussian line-shape with half-width-at-half-maximum (HWHM) of 0.12 eV. All spectra were normalized relative to the absorption maximum (i.e., the absorption maximum is set equal to one). Minimum energy configurations of **2** and **3** in their lowest triplet states were also obtained at the DFT/PBE0 level of theory, using the same combination of basis sets as described above. The character of singly occupied molecular orbitals was determined by using the natural orbital picture.[72]

Electron Transfer Dynamics Simulations. The simulations of IET were based on the model supercells of TiO_2 surfaces (101), functionalized with **1**, **2**, and **3** in vacuum. All initial structures were relaxed at the DFT/PBE (nanoparticle) and DFT/PBE0 (adsorbate) level of theory as described above. The time propagation of the electronic excitations was based on a tight-binding model Hamiltonian gained from the semiempirical extended Hückel method (eH).[9] We first solved the time-independent Schrödinger equation in the basis set of Slater-type atomic orbitals (AOs) $|\chi_i\rangle$,

$$\mathbf{HQ}^q = E_q \mathbf{SQ}^q \tag{1}$$

where **H** represents the extended Hückel Hamiltonian matrix, **S** is the atomic orbital overlap matrix, $\mathbf{Q}^q$ are the expansion coefficients of the molecular orbitals,

$$|q\rangle = \sum_i Q_i^q |\chi_i\rangle \tag{2}$$

and E_q are the corresponding eigenvalues. The initial state was expanded as a linear combination of the molecular orbitals,

$$|\Psi(0)\rangle = \sum_q C_q |q\rangle = \sum_q \sum_i C_q Q_i^q |\chi_i\rangle \tag{3}$$

Most initial states were defined as excited electronic states of the adsorbates that resulted from allowed optical transitions in the UV/Vis region and had significant electronic coupling with the semiconductor conduction band (i.e., electronic states where the excited electron occupies virtual orbitals of the adsorbate positioned within the conduction band).

The time-evolved wave function was obtained by propagating the initial state as follows,

$$|\Psi(t)\rangle = e^{-(i/\hbar)\hat{H}t}|\Psi(0)\rangle \quad (4)$$

where

$$|\Psi(t)\rangle = \sum_i \sum_q C_q Q_i^q e^{-(i/\hbar)E_q t}|\chi_i\rangle \quad (5)$$

$$|\Psi(t)\rangle = \sum_i B_i(t)|\chi_i\rangle \qquad B_i(t) = \sum_q C_q Q_i^q e^{-(i/\hbar)E_q t} \quad (6)$$

Finally, the time-evolved electronic wave function was projected onto the atomic orbitals of the molecular adsorbate to obtain the survival probability $P(t)$:

$$P(t) = |\sum_i^{\text{ads.}} \sum_j^{\text{all}} B_i^*(t)\, B_j(t) S_{ij}| \quad (7)$$

where the summation over i runs through the atomic orbitals of the adsorbate, and the summation over j runs through the complete basis. $P(t)$ describes the probability that the photoexcited electron remains in the adsorbate molecule at time t after the photoexcitation of the system.

The IET simulations from **1** were performed by using the supercell **1**−TiO_2 with lattice vectors a = 10.35 Å and b = 15.33 Å and depth ∼10 Å optimized with VASP as described above. In the case of **2**−TiO_2 and **3**−TiO_2, the simulations were conducted on 3 × 3 supercell arrays (lattice vectors a = 31.04 Å, b = 46.00 Å). To avoid artificial recurrences in electron-transient populations, the calculations of charge injection included absorbing potentials at the boundaries of the supercell. These are imaginary potentials placed on the Ti d orbitals that fully absorb the probability flux and ensure the early time relaxation dynamics is converged relative to the size of the supercells.

Results and Discussion

The results are presented as follows. First, we report the IET dynamics in **1**−TiO_2, with **1** attached to the TiO_2 nanoparticle in monodentate and bidentate binding modes. These calculations determine the relative binding energies of the two attachment modes and compare their corresponding rates of IET. Next, we describe the IET dynamics in **2**−TiO_2 and **3**−TiO_2 using the covalent attachment mode with most favorable thermodynamics (binding energy) and kinetics (IET rate) factors. Simulations of IET provide us with the electron injection rates from various virtual orbitals. These individual rates are subsequently weighted according to the electronic transition dipole moments obtained from TD-DFT calculations. The resulting combination of simulations of IET and TD-DFT calculations allow us to predict the net rates and probabilities of IET into TiO_2.

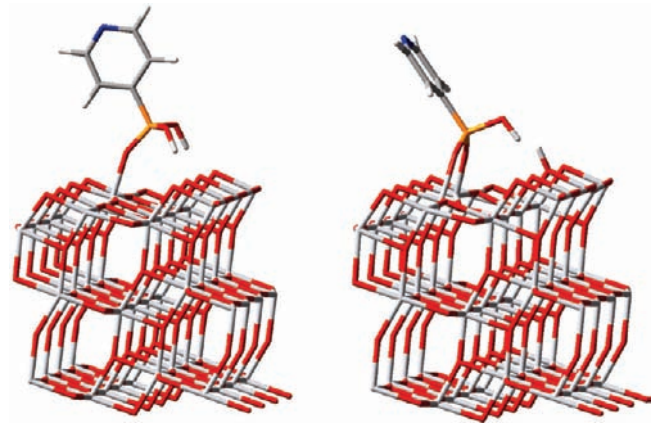

Figure 1. Model nanostructure after geometry relaxation of surface and pyridine-4-phosphonic acid in monodentate and bidentate modes.

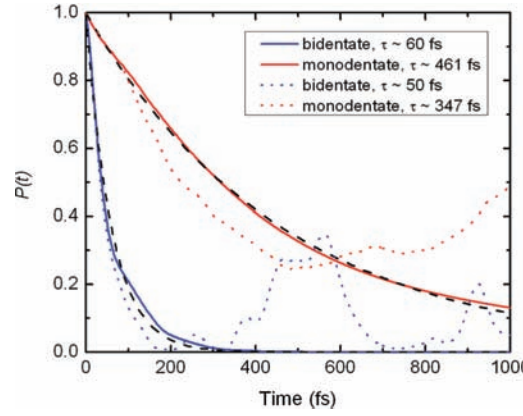

Figure 2. Survival probability for electron relaxation starting from the LUMO of the adsorbate for monodentate and bidentate attachment to TiO_2. Shown are results obtained without absorbing potentials (dotted lines) and with absorbing potentials (solid lines). Estimated rates for the simulations including the absorption potentials are plotted with black dashed lines.

Electron Injection from Pyridine. The pyridine-4-phosphonic acid (**1**) can be attached to a TiO_2 nanoparticle in monodentate and bidentate modes (see Figure 1) since these are the most stable adsorption modes for the phosphonate group.[46] The binding energies of these two modes differ by only 0.7 kcal/mol and are essentially identical at the level of theory being considered here. Our results are similar to those obtained by Nilsing et al.,[50] who determined the monodentate binding mode to be more stable by 5.4 kcal/mol. The 4.7 kcal/mol difference between our results is probably caused by the use of different functionals (PBE vs B3LYP). Therefore, both attachment modes were studied to compare their relative impedances.

Figure 2 compares the IET dynamics in **1**−TiO_2 when **1** is attached to TiO_2 in monodentate and bidentate binding modes after $\pi \rightarrow \pi^*$ excitation of the pyridine moiety (i.e., considering electron injection from the pyridine LUMO). It is shown that electron injection is significantly faster (τ_{inj} = 60 fs) for the bidentate binding mode than for monodentate binding (τ_{inj} = 461 fs). It is worth noting that the electron injection times obtained from the simulations, which did not include absorbing potentials are slightly faster, τ_{inj} = 50 fs for the bidentate binding mode and τ_{inj} = 347 fs for the monodentate binding mode. One can, however, observe artificial recurrences in electron-transient populations in these simulations (see Figure 2) due to the finite size of the TiO_2 nanoparticle.

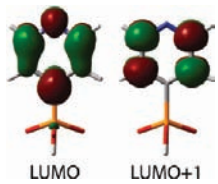

Figure 3. LUMO and LUMO+1 orbitals of pyridine adsorbate.

The difference in the injection rates of the two attachment modes is likely due to the presence of two P−O−Ti bridges, functioning as injection channels in the bidentate binding mode versus only one P−O−Ti bridge in the monodentate binding mode. Additionally, the pyridine group in the bidentate attachment is rotated by approximately 90° with respect to the phosphonate linker. On the basis of our preliminary calculations, in which we rotated the pyridine group by 90° for both monodentate and bidentate attachments, rotation of the pyridine group does not have any significant effect on the calculated electron injection rates. These results are quite intriguing, since such rotation of pyridine ring, when attached to ZnO by carboxylic acid group, leads to complete decoupling of the pyridine and carboxylic acid subunits and thus significant decrease in the injection rate.[54] This points toward some differences between the phosphonic and carboxylic acid anchor groups and further work is needed to investigate these more closely.

Overall, our results suggest that both phosphonic acid attachment modes are expected to have comparable stability but different kinetics of IET, with significant lower impedance for the bidentate attachment. Therefore, our studies of IET dynamics in **2**−TiO_2 and **3**−TiO_2 are focused on model supercells where **2** and **3** are covalently attached to TiO_2 according to the bidentate attachment motif.

We have also investigated IET from LUMO+1 of **1**−TiO_2 in both monodentate and bidentate binding modes. The IET is an order of magnitude slower ($\tau_{inj} \sim 1.3$ ps for monodentate attachment, $\tau_{inj} \sim 2.2$ ps for bidentate attachment) starting from the LUMO+1 initial state versus the LUMO initial state for both modes of attachment. This is due to the node in the electronic density occurring at the carbon atom of the pyridine ring that is functionalized with the phosphonic acid linker (see Figure 3), which reduces the coupling with the electronic states on the surface. Similar differences between the coupling of LUMO and LUMO+1 of pyridine-4-phosphonic acid with TiO_2 were noted in the work of Nilsing and co-workers.[50]

Electron injection times due to IET in **1**−TiO_2 were previously estimated from the full width at half-maximum (FWHM) associated with the initial state (i.e., the pyridine LUMO) projected onto the total DOS of **1**−TiO_2 ($\tau_{inj} = \hbar$/FWHM, as a variation of Newns−Anderson approach).[73,74] The estimation based on the DFT B3LYP calculation predicted $\tau_{inj} = 35$ fs, and $\tau_{inj} = 32$ fs, for monodentate and attachment modes, respectively.[50] We obtained similar results by using the DOS based on the semiempirical extended Hückel method (eH), predicting approximately the same injection time for the bidentate attachment ($\tau_{inj} = 26$ fs) and twice as slow injection time for the monodentate attachment ($\tau_{inj} = 80$ fs). In contrast to this, explicit simulations of IET predict a slightly slower injection time for the bidentate mode and an order of magnitude slower injection ($\tau_{inj} = 461$ ps) for the monodentate attachment, pointing out limitations of the approximate analysis based on $\tau_{inj} = \hbar$/FWHM. Results obtained with different methodologies are summarized in Table 1.

Recently, Li et al.[75] performed explicit simulations of IET for **1**−TiO_2 in monodentate attachment based on a model Hamiltonian with parameters determined from DFT B3LYP calculations. Interestingly, their simulations predict injection time $\tau_{inj} = 11$ fs, approximately 3 times faster than the injection time estimated from the DOS based on the B3LYP calculations and significantly faster than the injection time determined in this work ($\tau_{inj} = 461$ fs). An obvious difference between the two explicit dynamics studies is the level of theory considered (DFT B3LYP vs eH). Furthermore, Li et al. used a finite $(TiO_2)_{46}$ cluster as a model of the metal oxide surface rather than a nanoparticle derived from the PBC studies. Differences in the optimized geometries between the cluster and nanoparticle optimized using PBC could lead to the differences in the electronic structure at the adsorbate−nanoparticle interface and hence the adsorbate−nanoparticle coupling, thus influencing the electron injection rate. Moreover, IET in **1**−TiO_2 in the bidentate attachment was not investigated in their work, making it difficult to further assess the origin of these differences.

TABLE 1: Comparison of Characteristic Times (τ_{inj}) for the Electron Injection Process Obtained from Different Methodologies

1−TiO_2 adsorption mode	monodentate	bidentate
eH: $\hbar$/FWHM[a]	80.3 fs	26.0 fs
eH: dynamics[a]	461.4 fs	60.1 fs
B3LYP: $\hbar$/FWHM[b]	35 fs	32 fs
B3LYP: dynamics[c]	11.3 fs	

[a] This work. [b] Refrence 50. [c] Reference 75.

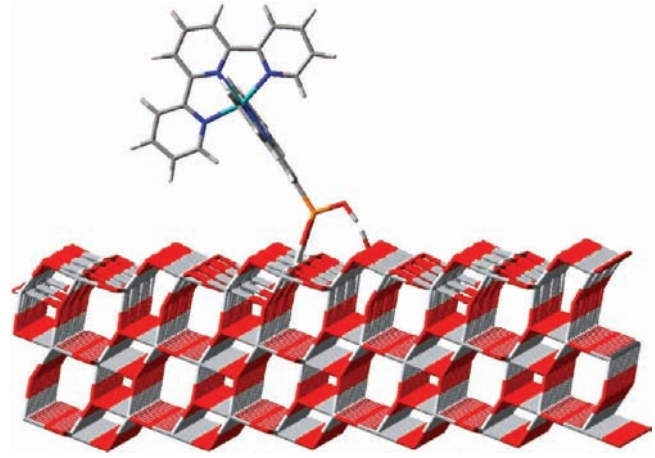

Figure 4. $[Ru(tpy)(tpy(PO_3H_2))]^{2+}$ in the bidentate binding mode on a 3 × 3 slab of TiO_2.

Electron Injection from the Sensitizer $[Ru(tpy)(tpy(PO_3H_2))]^{2+}$. *Results of the IET Simulations.* The sensitizer $[Ru(tpy)_2]^{2+}$ was functionalized with a phosphonic acid linker, $[Ru(tpy)(tpy(PO_3H_2))]^{2+}$ (**2**), and attached to the TiO_2 nanoparticle in a bidentate mode (see Figure 4). The density of states (DOS) obtained by the extended Hückel (eH) method for **2** adsorbed on TiO_2 is presented in Figure 5. The DOS plot shows the presence of energy levels from the adsorbate in the bandgap of TiO_2. Additionally, there is a number of virtual orbitals (LUMO through LUMO+13) positioned within the conduction band. These are the adsorbate orbitals that, upon photoexcitation, are responsible for promoting the IET. Virtual molecular orbitals representative of the various types of spatial distribution and symmetry, can be seen in Figure 6.

Several of the orbitals positioned in the conduction band (LUMO, LUMO+2, LUMO+3, LUMO+5, LUMO+7, LUMO+8, LUMO+10, and LUMO+13) have significant electron population on the tpy(PO_3H_2) ligand. These orbitals have

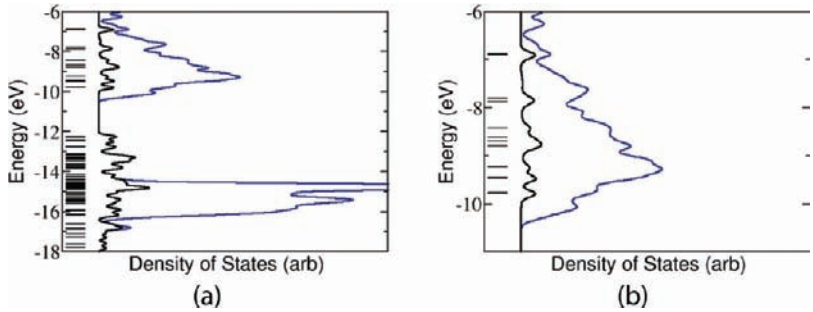

Figure 5. Density of states (DOS) obtained from the extended Hückel method for the $[Ru(tpy)(tpy(PO_3H_2))]^{2+}$−anatase model nanostructure. (a) shows the valence and conduction bands; (b) shows the expanded conduction band. In both plots, blue line shows the total DOS and black line represents the projected DOS onto the adsorbate orbitals. The level set lines give the molecular orbital energies of the free adsorbate in vacuum. DOS is convoluted with a Gaussian function (FWHM = 0.1 eV).

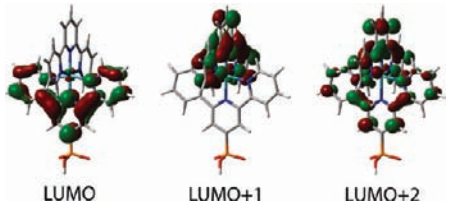

Figure 6. Virtual molecular orbitals obtained from extended Hückel theory.

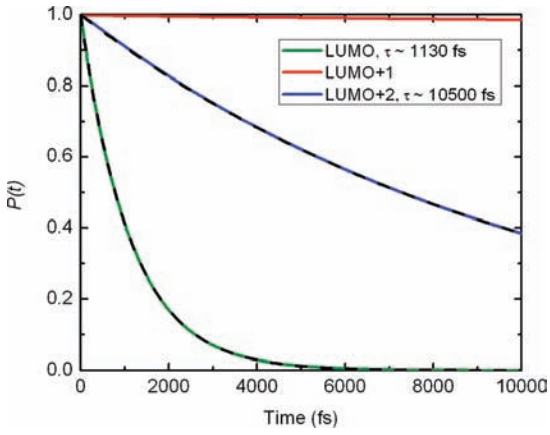

Figure 7. Survival probability for electron relaxation starting from the LUMO, LUMO+1, and LUMO+2 virtual orbitals of the $[Ru(tpy)(tpy(PO_3H_2))]^{2+}$ adsorbate. An estimated rate is plotted with the black dashed line.

relatively strong electronic coupling with the conduction band of TiO_2 and can promote efficient interfacial electron transfer. Ignoring the linker and assuming C_{2v} symmetry for the tpy ligand, LUMO, LUMO+5, and LUMO+10 orbitals belong to b_1 symmetry species and are similar in character to the LUMO of pyridine (cf. Figure 3), while LUMO+2, LUMO+3, LUMO+7, LUMO+8, and LUMO+13 have a_2 symmetry and are similar to the LUMO+1 of pyridine. Adsorbate orbitals with b_1 symmetry give an IET rate of approximately 1 ps, while those with a_2 symmetry give an IET rate of ∼10 ps (see Figure 7). These findings fit well with the results of IET simulations on **1**−TiO_2, where electron injection from the LUMO initial state is 1 order of magnitude faster than the injection from LUMO+1 initial state. Interestingly, all orbitals have minimal electron population on the phosphonic acid linker. This is probably responsible for the slower IET rate observed for dyes attached to TiO_2 via the phosphonic acid linker compared to the carboxylic acid linker.

Lundqvist et al.[48] estimated the electron injection rate using the Newns−Anderson approach[73,74] from LUMO of **2** into a nanocrystalline TiO_2 to be 65 fs, which is 2 orders of magnitude faster than the electron injection rate determined by our calculations. As mentioned above, the two methodologies are intrinsically different as the Newns−Anderson approach is based on the Fermi's Golden rule. On the other hand, we have carried out the actual time evolution of the initial wavepacket localized on the adsorbate LUMO. Both our and Newns−Anderson approaches ignore electron−phonon coupling and reorganization energies.

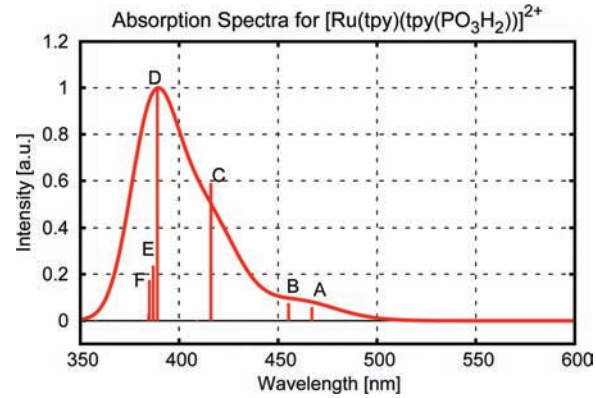

Figure 8. Absorption spectra of $[Ru(tpy)(tpy(PO_3H_2))]^{2+}$ obtained with TD-DFT.

Experimental measurements[18] performed on donor−Ru(II) bisterpyridine−phosphonic acid−nanocrystalline TiO_2 assembly suggest that the electron transfer from the terpyridine group attached to the semiconductor is very fast, with a rate <1 ns, which is in agreement with the 1 to 10 ps injection times calculated here.

Our calculations of injection times for the virtual orbitals with the electron population on the second terpyridine ligand not attached to TiO_2 (LUMO+1, LUMO+6, LUMO+11, LUMO+12) and those with the electron population on the Ru d orbitlal (LUMO+4 and LUMO+9) indicate that either those orbitals do not inject or the time scale is much slower, as no significant adsorbate electron population loss was observed.

States Populated upon Photoexcitation. The simulated absorption spectrum in the visible region for free $[Ru(tpy)(tpy(PO_3H_2))]^{2+}$, obtained by the TD-DFT formalism, is shown in Figure 8. The shape and the main peaks of the spectra reproduce the experimental data[35] reasonably well, although the peaks are shifted by about 0.5 eV to higher energies. Such peak shifts are not uncommon for TD-DFT calculations.[76] One should also keep in mind that our calculations were performed in a vacuum with the phosphonic acid attached to one of the terpyridine groups, while the experimental data was obtained for $[Ru(tpy)_2]^{2+}$ in solution (acetonitrile), which can stabilize

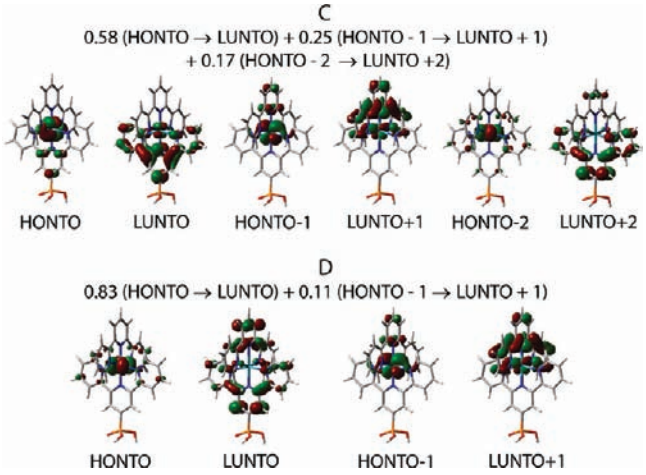

Figure 9. Natural transition orbitals for the most intense excitations of free $[Ru(tpy)(tpy(PO_3H_2))]^{2+}$. Labels C and D correspond to the labeling of absorption peaks in Figure 8. HONTO stands for the highest occupied natural transition orbital, and LUNTO stands for the lowest unoccupied natural transition orbital.

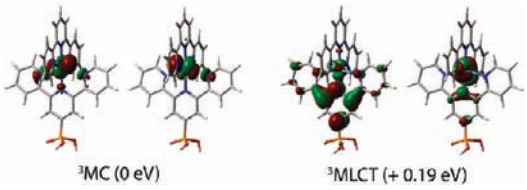

Figure 10. Singly occupied natural orbitals and relative energies of ^{3}MC and ^{3}MLCT states of $[Ru(tpy)(tpy(PO_3H_2))]^{2+}$ optimized in vacuum.

the MLCT excited states and can account for some of the peak shift and slightly different features of the spectra. The most intense peaks, represented by excitations C and D in Figure 8, correspond to the excitation of a particle into the orbitals with electron density on the $tpy(PO_3H_2)$ ligand. Natural transition orbitals (NTOs) corresponding to these excitations are shown in Figure 9. The particle for excitation C is mainly located on the orbital with b_1 symmetry, which would indicate a possibility of electron injection into the TiO_2 nanoparticle at ~1 ps time scale. In the case of excited state D, the particle is mainly located on an orbital which has a_2 symmetry, indicating the time scale for the electron injection in this case to be at the slower, 10 ps, time scale. In this line of reasoning, excited state A will inject at the 1 ps time scale and excited state F will inject at 10 ps time scale. Excited states B and E will not lead to the electron injection into TiO_2, since they have no significant population on the $tpy(PO_3H_2)$ ligand.

Electron injection from the adsorbate does not need to necessarily occur from the optically active excited states. $[Ru(tpy)_2]^{2+}$ in an excited singlet state can undergo intersystem crossing into the lowest triplet excited state. The two lowest triplet excited states of **2** are shown in Figure 10. Our calculations predict that these two states are very close in energy, with the ^{3}MC (metal centered) state being lower by only 4 kcal/mol. On the basis of IET simulations, the ^{3}MC state does not lead to the electron injection into TiO_2, while the ^{3}MLCT state will inject an electron into TiO_2 on a 1 ps time scale. Since emission from the ^{3}MLCT state of $[Ru(tpy)_2]^{2+}$ has been observed experimentally with a lifetime of 250 ps at room temperature,[35] one would expect this state to be populated in the case of **2** as well. Moreover, since the time scale for IET is two orders of magnitude smaller than the recombination lifetime,

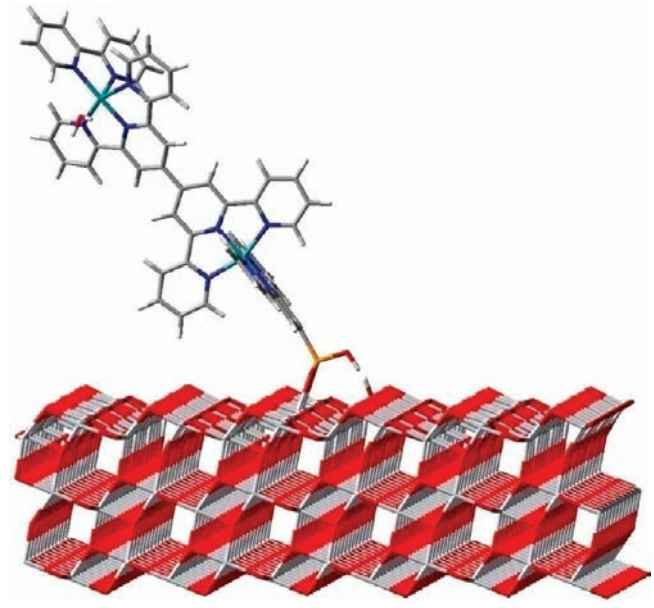

Figure 11. $[Ru(tpy)(bpy)(H_2O)-Ru(tpy)(tpy(PO_3H_2))]^{4+}$ on a 3 × 3 slab of TiO_2.

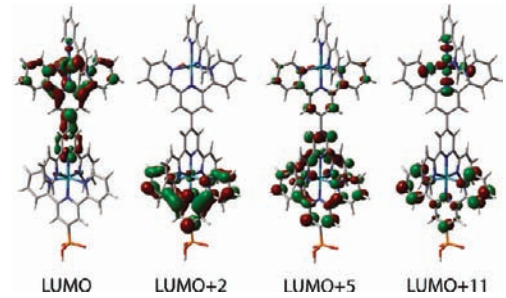

Figure 12. Virtual molecular orbitals of $[Ru(tpy)(bpy)(H_2O)-Ru(tpy)(tpy(PO_3H_2))]^{4+}$ obtained from extended Hückel theory.

the electron injection will also be competitive with the decay back to the ground state.

Electron Injection from the Molecular Assembly $[Ru(tpy)_2-Ru(tpy)(bpy)(H_2O)]^{4+}$. Results of the IET Simulations. Electron injection from $[Ru(tpy)(bpy)(H_2O)-Ru(tpy)(tpy(PO_3H_2))]^{4+}$ (**3**) into the TiO_2 nanoparticle was studied in the bidentate binding mode (see Figure 11). As in the case of **2**, attachment of **3** to the nanoparticle introduces a number of states (LUMO through LUMO+19) in the conduction band of TiO_2. We have performed simulations of the interfacial electron transfer from each of these virtual orbitals. Some representative virtual molecular orbitals are shown in Figure 12.

Eight of the virtual orbitals positioned in the conduction band (LUMO+2, LUMO+5, LUMO+6, LUMO+7, LUMO+11, LUMO+12, LUMO+13, and LUMO+16) have significant electron population on the terpyridine ligand covalently attached to TiO_2 through the phosphonic acid linker. These are the orbitals that promote interfacial electron transfer. Assuming C_{2v} symmetry for the tpy ligand, virtual orbitals with electron population on the $tpy(PO_3H_2)$ ligand can be again divided into two groups: those that belong to b_1 symmetry (LUMO+2, LUMO+11, LUMO+12) and those with a_2 symmetry (LUMO+5, LUMO+6, LUMO+7, LUMO+13, LUMO+16). Representative plots of the electron injection dynamics from the molecular assembly to the TiO_2 surface are shown in Figure 13. The fastest IET rate, ~1 ps, is observed for the LUMO+2 orbital. IET rates from orbitals LUMO+11 and LUMO+12 have nonexponential probabilities. This is due to the fact that the

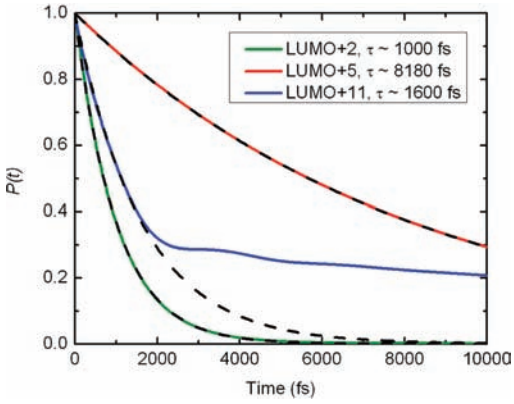

Figure 13. Survival probability for electron relaxation starting from the LUMO+2, LUMO+5, and LUMO+11 virtual orbitals of the $[Ru(tpy)(bpy)(H_2O)-Ru(tpy)(tpy(PO_3H_2))]^{4+}$ adsorbate. An estimated rate is plotted with the black dashed line.

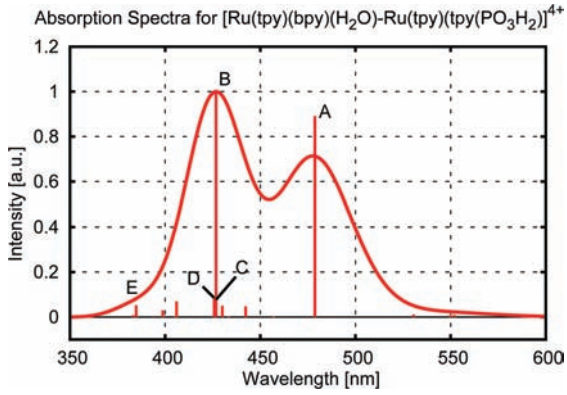

Figure 14. Absorption spectra of $[Ru(tpy)(bpy)(H_2O)-Ru(tpy)(tpy(PO_3H_2))]^{4+}$ obtained with TD-DFT.

electron is delocalized over both $[Ru(tpy)(tpy(PO_3H_2)]^{2+}$ and $[Ru(tpy)(bpy)(H_2O)]^{2+}$ subunits and only the charge density on the terpyridine ligand covalently bound to the semiconductor couples with the states in the conduction band leading to injection (see Figure 13). The rates of electron injection from orbitals belonging to the a2 symmetry are approximately 7−21 ps.

Virtual orbitals with electron population on the tpy−tpy bridge (LUMO, LUMO+1, LUMO+4, LUMO+9), Ru(tpy)(bpy)(H_2O) moiety (LUMO+3, LUMO+14, LUMO+17), or on the d orbital of Ru atom in $Ru(tpy)_2$ (LUMO+8, LUMO+18), have no observable adsorbate electron population loss on the 10 ps time scale considered in this work. Interestingly, orbitals with relatively high energy and electron density localized on the tpy−tpy bridge (LUMO+15 and LUMO+19) will inject electron into TiO_2 with the rate of ∼50 ps.

States Populated upon Photoexcitation. The simulated absorption spectrum for $[Ru(tpy)(bpy)(H_2O)-Ru(tpy)(tpy(PO_3H_2))]^{4+}$ (**3**) is shown in Figure 14. The two most intense peaks, A and B, correspond to excitations from the ruthenium d orbitals, to the bridging tpy−tpy group (see Figure 15). On the basis of our IET simulations, these excited states will not lead to the electron injection into TiO_2, since they have no significant electron population on the tpy(PO_3H_2) ligand attached to the nanoparticle. Among all other excited states in the visible region, only excitations C, D, and E have significant electron population on the tpy(PO_3H_2) ligand favoring the IET.

As in the case of the $[Ru(tpy)_2]^{2+}$ molecule, $[Ru(tpy)(bpy)(H_2O)-Ru(tpy)_2]^{4+}$ can also undergo intersystem crossing

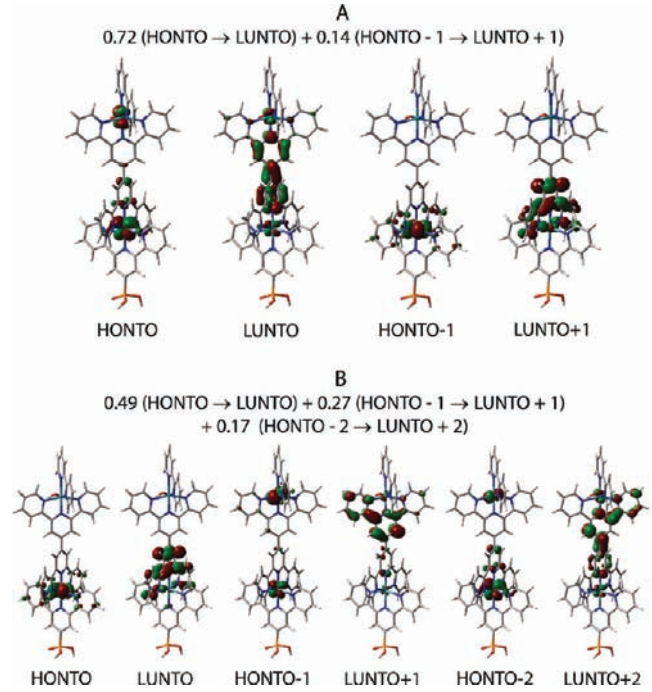

Figure 15. Natural transition orbitals for the most intense excitations of free $[Ru(tpy)(bpy)(H_2O)-Ru(tpy)(tpy(PO_3H_2))]^{4+}$. Labels A and B correspond to the labeling of absorption peaks in Figure 14. HONTO stands for the highest occupied natural transition orbital and LUNTO stands for the lowest unoccupied natural transition orbital.

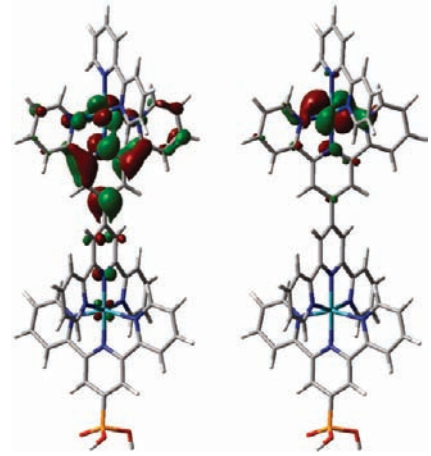

Figure 16. Singly occupied natural orbitals of lowest triplet excited state of $[Ru(tpy)(bpy)(H_2O)-Ru(tpy)(tpy(PO_3H_2))]^{4+}$ optimized in vacuum.

into the lowest triplet excited state. Singly occupied natural orbitals of the lowest triplet state are shown in Figure 16. On the basis of our IET simulations, this state will not lead to the electron injection into TiO_2 as there is no significant electron population on the tpy(PO_3H_2) ligand.

On the basis of the picture of singlet excited states and the lowest triplet excited state of $[Ru(tpy)(bpy)(H_2O)-Ru(tpy)(tpy(PO_3H_2))]^{4+}$, we suggest that, upon photoexcitation, interfacial electron transfer from the molecular assembly to the semiconductor surface will occur with low probability. This is the result of the localization of the excited electron on the tpy−tpy bridge, which does not have favorable electronic coupling with the TiO_2 nanoparticle.

It is important to note here that our calculations do not take into account vibrational effects. Therefore, the possibility of the electron injection from the tpy−tpy localized excited state cannot

be ruled out as there might be vibrational degrees of freedom coupled to the electron motion through the molecule.

Conclusions

In this work we have investigated interfacial electron transfer from a series of molecules: pyridine, $[Ru(tpy)_2]^{2+}$, and $[Ru(tpy)_2-Ru(tpy)(bpy)(H_2O)]^{4+}$, adsorbed on the (101) surface of anatase TiO_2 using a phosphonic acid linker. The IET rates we obtained from full quantum dynamics simulations with an extended Hückel Hamiltonian are significantly slower than those obtained by a Newns−Anderson approach.

Simulations of electron injection from **1** attached to the anatase TiO_2 showed that the IET is faster when the phosphonic acid is attached to the surface in bidentate mode. We attribute this to the presence of two P−O−Ti bridges in the bidentate binding mode versus one P−O−Ti bridge in the monodentate binding mode, since the electron transfer from adsorbate into the nanoparticle occurs mainly through the P−O−Ti bridge. The IET is an order of magnitude faster starting from the LUMO initial state versus the LUMO+1 initial state for both modes of attachment. This is due to the node in the electronic density occurring at the carbon atom of the pyridine ring that is functionalized with the phosphonic acid linker.

Electron injection simulations coupled with TD-DFT calculations on $[Ru(tpy)(tpy(PO_3H_2))]^{2+}$ suggest that the most intense singlet excited states will undergo IET with a rate of 1 or 10 ps, depending on the orbital symmetry of the excited state. The lowest triplet excited state with MLCT character will undergo IET with the rate of ∼1 ps. This electron injection rate is competitive with the ^{3}MLCT decay into the ground state, which occurs on an approximately 250 ps time scale at room temperature.[35] Excited states involving electron excitation into the d orbital of Ru or the terpyridine ligand away from the TiO_2 surface will not undergo IET.

We did not observe IET on the time scale considered in this work for the most intense excited states and the lowest triplet excited state of $[Ru(tpy)(bpy)(H_2O)-Ru(tpy)(tpy(PO_3H_2))]^{4+}$. This is due to the fact that the excited electron is localized on the tpy−tpy bridge, which does not have favorable coupling with the TiO_2 nanoparticle. This state could, in principle, couple to a more favorable state via phonons. However, one would expect a slower injection rate. Even in the framework of our approximation there is a possibility for IET, albeit with a low probability, as some of the higher excited states with low intensity display significant electron population on the $tpy(PO_3H_2)$ ligand.

These findings have implications for design of artificial photocatalysts, especially when electron injection into the metal oxide semiconductor is desirable. It is important to design molecular assemblies in a way that, upon initial excitation, favors electron localization on the ligands with strong electronic coupling to the semiconductor. In the context of our catalyst−chromophore model system, modifications to the tpy−tpy bridging ligand are needed, which would make it less electron accepting and thereby favor electron excitations into the $tpy(PO_3H_2)$ ligand. Alternatively, one could substitute electron withdrawing groups on the $tpy(PO_3H_2)$ ligand to achieve favorable electron localization.

Acknowledgment. R.S. thanks the Center for Nonlinear Studies at Los Alamos National Laboratory for summer research fellowship. This work was supported by the Laboratory Directed Research and Development (LDRD) program at Los Alamos National Laboratory. Los Alamos National Laboratory is operated by Los Alamos National Security, LLC, for the National Nuclear Security Administration of the U.S. Department of Energy under contract DE-AC52-06NA25396. V.S.B. acknowledges supercomputer time from NERSC and support from the DOE grant DE-FG02-07ER15909 and the NSF grant ECCS-0404191.

References and Notes

(1) Roundhill, D. M. Photochemistry, photophysics, and photoredox reactions of $Ru(bpy)_3^{2+}$ and related complexes. In *Photochemistry and photophysics of metal complexes*; Plenum Press: New York, 1994; p 165.
(2) Batista, E. R.; Martin, R. L. *J. Am. Chem. Soc.* **2007**, *129*, 7224.
(3) Li, G.; Sproviero, E. M.; Snoeberger, R. C., III; Iguchi, N.; Blakemore, J. D.; Crabtree, R. H.; Brudvig, G. W.; Batista, V. S. *Energy Environ. Sci.* **2009**, *2*, 230.
(4) Iguchi, N.; Cady, C.; Snoeberger, R. C., III; Hunter, B. M.; Sproviero, E. M.; Schmuttenmaer, C. A.; Crabtree, R. H.; Brudvig, G. W.; Batista, V. S. *Proc. SPIE* **2008**, *7034*, 70340C.
(5) McNamara, W. R.; Snoeberger, R. C.; Li, G.; Schleicher, J. M.; Cady, C. W.; Poyatos, M.; Schmuttenmaer, C. A.; Crabtree, R. H.; Brudvig, G. W.; Batista, V. S. *J. Am. Chem. Soc.* **2008**, *130*, 14329.
(6) Abuabara, S. G.; Cady, C. W.; Baxter, J. B.; Schmuttenmaer, C. A.; Crabtree, R. H.; Brudvig, G. W.; Batista, V. S. *J. Phys. Chem. C* **2007**, *111*, 11982.
(7) Sproviero, E. M.; Gascon, J. A.; McEvoy, J. P.; Brudvig, G. W.; Batista, V. S. *J. Inorg. Biochem.* **2006**, *100*, 786.
(8) Abuabara, S. G.; Rego, L. G. C.; Batista, V. S. *J. Am. Chem. Soc.* **2005**, *127*, 18234.
(9) Rego, L. G. C.; Batista, V. S. *J. Am. Chem. Soc.* **2003**, *125*, 7989.
(10) Bach, U.; Lupo, D.; Comte, P.; Moser, J. E.; Weissortel, F.; Salbeck, J.; Spreitzer, H.; Gratzel, M. *Nature* **1998**, *395*, 583.
(11) Hagfeldt, A.; Gratzel, M. *Chem. Rev.* **1995**, *95*, 49.
(12) O'Regan, B.; Gratzel, M. *Nature* **1991**, *353*, 737.
(13) Zakeeruddin, S. M.; Nazeeruddin, M. K.; Pechy, P.; Rotzinger, F. P.; HumphryBaker, R.; Kalyanasundaram, K.; Gratzel, M.; Shklover, V.; Haibach, T. *Inorg. Chem.* **1997**, *36*, 5937.
(14) Argazzi, R.; Bignozzi, C. A.; Heimer, T. A.; Castellano, F. N.; Meyer, G. J. *J. Am. Chem. Soc.* **1995**, *117*, 11815.
(15) Argazzi, R.; Bignozzi, C. A.; Heimer, T. A.; Castellano, F. N.; Meyer, G. J. *J. Phys. Chem. B* **1997**, *101*, 2591.
(16) Islam, A.; Sugihara, H.; Arakawa, H. *J. Photochem. Photobiol., A* **2003**, *158*, 131.
(17) Katoh, R.; Furube, A.; Kasuya, M.; Fuke, N.; Koide, N.; Han, L. *J. Mater. Chem.* **2007**, *17*, 3190.
(18) Bonhote, P.; Moser, J. E.; Humphry-Baker, R.; Vlachopoulos, N.; Zakeeruddin, S. M.; Walder, L.; Gratzel, M. *J. Am. Chem. Soc.* **1999**, *121*, 1324.
(19) Beley, M.; Bignozzi, C. A.; Kirsch, G.; Alebbi, M.; Raboin, J. C. *Inorg. Chim. Acta* **2001**, *318*, 197.
(20) Duprez, V.; Biancardo, M.; Krebs, F. C. *Sol. Energy Mater. Sol. Cells* **2007**, *91*, 230.
(21) Figgemeier, E.; Aranyos, V.; Constable, E. C.; Handel, R. W.; Housecroft, C. E.; Risinger, C.; Hagfeldt, A.; Mukhtar, E. *Inorg. Chem. Commun.* **2004**, *7*, 117.
(22) Nazeeruddin, M. K.; Kay, A.; Rodicio, I.; Humphry-Baker, R.; Mueller, E.; Liska, P.; Vlachopoulos, N.; Graetzel, M. *J. Am. Chem. Soc.* **1993**, *115*, 6382.
(23) Zabri, H.; Gillaizeau, I.; Bignozzi, C. A.; Caramori, S.; Charlot, M.-F.; Cano-Boquera, J.; Odobel, F. *Inorg. Chem.* **2003**, *42*, 6655.
(24) Falkenstrom, M.; Johansson, O.; Hammarstrom, L. *Inorg. Chim. Acta* **2007**, *360*, 741.
(25) Yang, X.; Baik, M. H. *J. Am. Chem. Soc.* **2006**, *128*, 7476.
(26) Yang, X. F.; Baik, M. H. *J. Am. Chem. Soc.* **2004**, *126*, 13222.
(27) Hurst, J. K. *Coord. Chem. Rev.* **2005**, *249*, 313.
(28) Yamada, H.; Siems, W. F.; Koike, T.; Hurst, J. K. *J. Am. Chem. Soc.* **2004**, *126*, 9786.
(29) Cape, J. L.; Hurst, J. K. *J. Am. Chem. Soc.* **2008**, *130*, 827.
(30) Hurst, J. K.; Cape, J. L.; Clark, A. E.; Das, S.; Qin, C. *Inorg. Chem.* **2008**, *47*, 1753.
(31) Ghanem, R.; Xu, Y. H.; Pan, J.; Hoffmann, T.; Andersson, J.; Polivka, T.; Pascher, T.; Styring, S.; Sun, L. C.; Sundstrom, V. *Inorg. Chem.* **2002**, *41*, 6258.
(32) Wolpher, H.; Sinha, S.; Pan, J. X.; Johansson, A.; Lundqvist, M. J.; Persson, P.; Lomoth, R.; Bergquist, J.; Sun, L. C.; Sundstrom, V.; Akermark, B.; Polivka, T. *Inorg. Chem.* **2007**, *46*, 638.
(33) Treadway, J. A.; Moss, J. A.; Meyer, T. J. *Inorg. Chem.* **1999**, *38*, 4386.
(34) She, C.; Guo, J.; Irle, S.; Morokuma, K.; Mohler, D. L.; Zabri, H.; Odobel, F.; Youm, K.-T.; Liu, F.; Hupp, J. T.; Lian, T. *J. Phys. Chem. A* **2007**, *111*, 6832.

(35) Sauvage, J. P.; Collin, J. P.; Chambron, J. C.; Guillerez, S.; Coudret, C.; Balzani, V.; Barigelletti, F.; Decola, L.; Flamigni, L. *Chem. Rev.* **1994**, *94*, 993.
(36) Asbury, J. B.; Anderson, N. A.; Hao, E.; Ai, X.; Lian, T. *J. Phys. Chem. B* **2003**, *107*, 7376.
(37) Hannappel, T.; Burfeindt, B.; Storck, W.; Willig, F. *J. Phys. Chem. B* **1997**, *101*, 6799.
(38) Kallioinen, J.; Benko, G.; Sundstrom, V.; Korppi-Tommola, J. E. I.; Yartsev, A. P. *J. Phys. Chem. B* **2002**, *106*, 4396.
(39) Benko, G.; Kallioinen, J.; Korppi-Tommola, J. E. I.; Yartsev, A. P.; Sundstrom, V. *J. Am. Chem. Soc.* **2002**, *124*, 489.
(40) Anderson, N. A.; Lian, T. *Annu. Rev. Phys. Chem.* **2005**, *56*, 491.
(41) Asbury, J. B.; Wang, Y.-Q.; Hao, E.; Ghosh, H. N.; Lian, T. *Res. Chem. Intermed.* **2001**, *27*, 393.
(42) Moyer, B. A.; Thompson, M. S.; Meyer, T. J. *J. Am. Chem. Soc.* **1980**, *102*, 2310.
(43) Han, F. S.; Higuchi, M.; Kurth, D. G. *J. Am. Chem. Soc.* **2008**, *130*, 2073.
(44) Houarner-Rassin, C.; Chaignon, F.; She, C.; Stockwell, D.; Blart, E.; Buvat, P.; Lian, T.; Odobel, F. *J. Photochem. Photobiol., A* **2007**, *192*, 56.
(45) Gillaizeau-Gauthier, I.; Odobel, F.; Alebbi, M.; Argazzi, R.; Costa, E.; Bignozzi, C. A.; Qu, P.; Meyer, G. J. *Inorg. Chem.* **2001**, *40*, 6073.
(46) Nilsing, M.; Lunell, S.; Persson, P.; Ojamae, L. *Surf. Sci.* **2005**, *582*, 49.
(47) Pechy, P.; Rotzinger, F. P.; Nazeeruddin, M. K.; Kohle, O.; Zakeeruddin, S. M.; HumphryBaker, R.; Gratzel, M. *J. Chem. Soc., Chem. Commun.* **1995**, 65.
(48) Lundqvist, M. J.; Nilsing, M.; Lunell, S.; Akermark, B.; Persson, P. *J. Phys. Chem. B* **2006**, *110*, 20513.
(49) Lundqvist, M. J.; Nilsing, M.; Persson, P.; Lunell, S. *Int. J. Quantum Chem.* **2006**, *106*, 3214.
(50) Nilsing, M.; Persson, P.; Ojamae, L. *Chem. Phys. Lett.* **2005**, *415*, 375.
(51) Persson, P.; Bergstrom, R.; Lunell, S. *J. Phys. Chem. B* **2000**, *104*, 10348.
(52) Persson, P.; Lundqvist, M. J. *J. Phys. Chem. B* **2005**, *109*, 11918.
(53) Persson, P.; Lundqvist, M. J.; Ernstorfer, R.; Goddard, W. A.; Willig, F. *J. Chem. Theory Comput.* **2006**, *2*, 441.
(54) Persson, P.; Lunell, S.; Ojamae, L. *Chem. Phys. Lett.* **2002**, *364*, 469.
(55) Kresse, G.; Furthmüller, J. *Phys. Rev. B* **1996**, *54*, 11169.
(56) Kresse, G.; Furthmüller, J. *Comput. Mater. Sci.* **1996**, *6*, 15.
(57) Perdew, J. P.; Burke, K.; Ernzerhof, M. *Phys. Rev. Lett.* **1996**, *77*, 3865.
(58) Blöchl, P. E. *Phys. Rev. B* **1994**, *50*, 17953.
(59) Kresse, G.; Joubert, D. *Phys. Rev. B* **1999**, *59*, 1758.
(60) Djerdj, I.; Tonejc, A. M. *J. Alloys Compd.* **2006**, *413*, 159.
(61) Ernzerhof, M.; Scuseria, G. E. *J. Chem. Phys.* **1999**, *110*, 5029.
(62) Frisch, M. J.; Trucks, G. W.; Schlegel, H. B.; Scuseria, G. E.; Robb, M. A.; Cheeseman, J. R.; Montgomery, J. A.; Vreven, J. T.; Kudin, K. N.; Burant, J. C.; Millam, J. M.; Iyengar, S. S.; Tomasi, J.; Barone, V.; Mennucci, B.; Cossi, M.; Scalmani, G.; Rega, N.; Petersson, G. A.; Nakatsuji, H.; Hada, M.; Ehara, M.; Toyota, K.; Fukuda, R.; Hasegawa, J.; Ishida, M.; Nakajima, T.; Honda, Y.; Kitao, O.; Nakai, H.; Klene, M.; Li, X.; Knox, J. E.; Hratchian, H. P.; Cross, J. B.; Bakken, V.; Adamo, C.; Jaramillo, J.; Gomperts, R.; Stratmann, R. E.; Yazyev, O.; Austin, A. J.; Cammi, R.; Pomelli, C.; Ochterski, J. W.; Ayala, P. Y.; Morokuma, K.; Voth, G. A.; Salvador, P.; Dannenberg, J. J.; Zakrzewski, V. G.; Dapprich, S.; Daniels, A. D.; Strain, M. C.; Farkas, O.; Malick, D. K.; Rabuck, A. D.; Raghavachari, K.; Foresman, J. B.; Ortiz, J. V.; Cui, Q.; Baboul, A. G.; Clifford, S.; Cioslowski, J.; Stefanov, B. B.; Liu, G.; Liashenko, A.; Piskorz, P.; Komaromi, I.; Martin, R. L.; Fox, D. J.; Keith, T.; Al-Laham, M. A.; Peng, C. Y.; Nanayakkara, A.; Challacombe, M.; Gill, P. M. W.; Johnson, B.; Chen, W.; Wong, M. W.; Gonzalez, C.; Pople, J. A. *Gaussian 03*; revision D.02; Gaussian, Inc.: Wallingford, CT, 2004.
(63) Hay, P. J.; Wadt, W. R. *J. Chem. Phys.* **1985**, *82*, 270.
(64) Roy, L. A.; Hay, P. J.; Martin, R. L. *J. Chem. Theory Comput.* **2008**, *4*, 1029.
(65) Hehre, W. J.; Ditchfield, R.; Pople, J. A. *J. Chem. Phys.* **1972**, *56*, 2257.
(66) Harihara, P. C.; Pople, J. A. *Theor. Chim. Acta* **1973**, *28*, 213.
(67) Bauernschmitt, R.; Ahlrichs, R. *Chem. Phys. Lett.* **1996**, *256*, 454.
(68) Casida, M. E.; Jamorski, C.; Casida, K. C.; Salahub, D. R. *J. Chem. Phys.* **1998**, *108*, 4439.
(69) Stratmann, R. E.; Scuseria, G. E.; Frisch, M. J. *J. Chem. Phys.* **1998**, *109*, 8218.
(70) Martin, R. L. *J. Chem. Phys.* **2003**, *118*, 4775.
(71) Batista, E. R.; Martin, R. L. Natural Transition Orbitals. *Encyclopedia of Computational Chemistry*; Wiley: Chichester, UK, 2004.
(72) Davidson, E. R. *Rev. Mod. Phys.* **1972**, *44*, 451.
(73) Muscat, J. P.; Newns, D. M. *Prog. Surf. Sci.* **1978**, *9*, 1.
(74) Anderson, P. W. *Phys. Rev.* **1961**, *124*, 41.
(75) Li, J.; Nilsing, M.; Kondov, I.; Wang, H.; Persson, P.; Lunell, S.; Thoss, M. *J. Phys. Chem. C* **2008**, *112*, 12326.
(76) Rappoport, D.; Furche, F. Excited States and Photochemistry. *Time-Dependent Density Functional Theory*; Springer: Berlin/Heidelberg, Germany, 2006; p 337.

JP903966N